ADVANCED FUNCTIONAL MATERIALS
www.afm-journal.de

Enhancing the Performance of Bi_2S_3 in Electrocatalytic and Supercapacitor Applications by Controlling Lattice Strain

*Hao Zhang, Jiefeng Diao, Mengzheng Ouyang, Hossein Yadegari, Mingxuan Mao, Jiaao Wang, Graeme Henkelman, Fang Xie, and David Jason Riley**

Lattice-strained Bi_2S_3 with 3D hierarchical structures are prepared through a top-down route by a topotactic transformation. High-resolution transmission electron microscopy and X-ray diffraction (XRD) confirm the lattice spacing is expanded by prolonged sulfuration. Performance studies demonstrate that Bi_2S_3 with the largest lattice expansion (Bi_2S_3-9.7%, where 9.7% represents the lattice expansion) exhibits a greater electrocatalytic hydrogen evolution reaction (HER) activity compared to Bi_2S_3 and Bi_2S_3-3.2%. Density functional theory calculations reveal the expansion of the lattice spacing reduces the bandwidth and upshifts the band center of the Bi 3*d* orbits, facilitating electron exchange with the S 2*p* orbits. The resultant intrinsic electronic configuration exhibits favorable H* adsorption kinetics and a reduced energy barrier for water dissociation in hydrogen evolution. Operando Raman and post-mortem characterizations using XRD and X-ray photoelectron spectroscopy reveal the generation of pseudo-amorphous Bi at the edge of Bi_2S_3 nanorods of the sample with lattice strain during HER, yielding Bi_2S_3-9.7%-A. It is worth noting when Bi_2S_3-9.7%-A is assembled as a positive electrode in an asymmetric supercapacitor, its performance is greatly superior to that of the same device formed using pristine Bi_2S_3-9.7%. The as-prepared Bi_2S_3-9.7%-A//activated carbon asymmetric supercapacitor achieves a high specific capacitance of 307.4 F g^{-1} at 1 A g^{-1}, exhibiting high retention of 84.1% after 10 000 cycles.

1. Introduction

Bismuth sulfide (Bi_2S_3) is a layered semiconductor with a direct bandgap of 1.3–1.7 eV.[1–3] The bismuth and sulfur atoms are connected by covalent bonds in a 2D layer, and 2D layers are connected by weak van der Waals forces.[4,5] The interlayer spacing of Bi_2S_3 is 0.32 nm, which is about half of that of MoS_2.[6] Bi_2S_3 has aroused great interest due to its high photoconductivity, good environmental compatibility, and abundant natural reserves.[7] However, up till now, Bi_2S_3 has been used in the field of photoelectrochemistry,[8] photoelectronics,[9] CO_2 reduction,[10,11] and nitrogen fixation,[12–14] and there is no research on the application of pure Bi_2S_3 in electrocatalytic hydrogen evolution reaction (HER).[15,16] Similar to MoS_2, due to the bismuth monoatomic layer sandwiched between two sulfur monoatomic layers in the 2D planar structure of Bi_2S_3, only the unsaturated sulfur edge atoms in Bi_2S_3 have proved catalytically active in photochemical applications, while the basal plane of the 2D structure is chemically inert.[17–19] This prevents Bi_2S_3 from contacting reactant molecules and greatly impacts its electrochemical performance.[20]

Applying lattice strain is an effective method to modify the internal interatomic distance, potentially increasing the contact with solvent molecules and changing the geometry and electronic structure of the active site, which helps to optimize electrocatalytic activity.[21,22] Due to the complex structure of inorganic metal sulfides and the difficulty of characterization, the lattice strain produced in previous studies of metal sulfides is usually related to structure mismatch, substrates induced or heteroatom substitution, and these factors make it difficult to identify strain-activity correlations.[23–26] However, the unique periodic layered structure and the loosely stacked framework with large open channels of Bi_2S_3 provide the opportunity of applying lattice strain without introducing the aforementioned factors.

Herein, a top-down route of topological transformation is described that permits the preparation of Bi_2S_3 with 3D multilevel architectures and different levels of strain. The influence of sulfuration time on lattice strain is determined using high-resolution transmission electron microscopy (HRTEM) and X-ray diffraction (XRD). The HER electrocatalytic activity

H. Zhang, H. Yadegari, F. Xie, D. J. Riley
Department of Materials and London Center for Nanotechnology
Imperial College London
London SW7 2AZ, UK
E-mail: jason.riley@imperial.ac.uk
J. Diao, J. Wang, G. Henkelman
Department of Chemistry and the Oden Institute for Computational Engineering and Sciences
The University of Texas at Austin
Austin, TX 78712, USA
M. Ouyang
Department of Earth Science and Engineering
Imperial College London
London SW7 2AZ, UK
M. Mao
Department of Electrical and Electronic Engineering
Imperial College London
London SW7 2AZ, UK

The ORCID identification number(s) for the author(s) of this article can be found under https://doi.org/10.1002/adfm.202205974.

DOI: 10.1002/adfm.202205974

of Bi_2S_3 samples with different lattice strain is investigated and rationalized with reference to X-ray photoelectron spectroscopy (XPS) and ultraviolet-visible spectroscopy (UV–vis) spectroscopy studies and density functional theory (DFT) calculations.

2. Results and Discussion

2.1. Structural Characterization and Chemical Analysis

2.1.1. Preparation and Lattice Strain Analysis

Bi_2S_3 hierarchical structures with lattice strain are synthesized via a topotactic transformation method, as illustrated in **Figure 1**a. The hierarchical BiOCOOH was prepared as a precursor, and it was sulfurized to yield Bi_2S_3 with similar architectures to the parent material. In this procedure, the crystal structure changes to that of Bi_2S_3 while the spatial morphology of the precursor is maintained, this is due to ion exchange of S^{2-} with O^{2-} and $COOH^-$ and lattice matching of BiOCOOH and Bi_2S_3. By prolonging the conversion time to Bi_2S_3, the interlayer interaction is weakened and the interlayer distance expanded, resulting in increased lattice expansion. Bi_2S_3 with different lattice strains is obtained by adjusting the sulfuration time.

Figure 1b displays a scanning electron microscopy (SEM) image of the hierarchical BiOCOOH assembled from interlaced nanosheets. Figure 1c–e is the SEM and HRTEM images of Bi_2S_3 with sulfuration times of 10, 12, and 14 h, respectively. It is seen from the SEM images that the Bi_2S_3 networks are interwoven by crossed nanorods with long-range order. As the sulfuration time increases from 10 to 14 h, the nanorods gradually become thinner, while the morphology remains essentially unchanged. When the sulfuration time is prolonged to 16 h, the interwoven structure of the Bi_2S_3 nanorods collapses (Figure S1, Supporting Information). From the HRTEM images of the sample sulfurized for 10 h (Figure 1c), a lattice spacing of 3.1 Å is attributed to the (211) planes of Bi_2S_3. When the sulfuration time is prolonged to 12 and 14 h, the corresponding lattice spacing is enlarged to 3.2 and 3.4 Å, which corresponds to lattice expansion ratios of 3.2% and 9.7%, respectively. The percentages of S measured by inductively coupled plasma mass spectrometry (ICP-MS) in Bi_2S_3, Bi_2S_3-3.2%, Bi_2S_3-9.7% are 18.3%, 21.9%, and 26.2%, respectively, indicating an increased S^{2-} percentage in the Bi_2S_3 samples with the increase of sulfuration time, which enhances the interlayer repulsion and weakens the van der Waals forces between Bi_2S_3 layers, resulting in increased layer mobility and lattice expansion, and decreased crystallinity. In addition, the Bi—S ratio in Bi_2S_3-9.7% is significantly lower than that of Bi_2S_3 from the energy-dispersive X-ray spectroscopy (STEM-EDS), which agrees with the ICP results, indicating an increase in the relative content of sulfur (Figure S2, Supporting Information).

Figure 1g displays the XRD patterns of the precursor and final products after sulfuration for 10 h, in which all the characteristic diffraction peaks are indexed to tetragonal BiOCOOH (JCPDS card No. 35–0939) and orthorhombic Bi_2S_3 (JCPDS card No.17-0320, a = 11.15 Å, b = 11.30 Å, c = 3.98 Å), respectively, indicating that the BiOCOOH is completely transformed to pure Bi_2S_3 crystal without lattice strain. A complete transformation is further confirmed by the disappearance of the peaks of C=O, C—OH, O—H, Bi—O bands and the appearance of Bi—S bands in the Fourier-transform infrared (FT-IR) spectra after sulfuration (Figure 1h).[27,28]

The XRD patterns of the Bi_2S_3 products with different sulfuration times are shown in Figure 1i, the characteristic reflection of the (211) plane at 29.1° of the Bi_2S_3 sulfurized for 10 h shifts down to 28.8° and 28.4° after the Bi_2S_3 is sulfurized for 12 and 14 h, which is lower than the expansion rate observed from HRTEM. As XRD patterns reflect the lattice strain of the entire bulk phase, while HRTEM images observe the lattice expansion on the surface of the material, this result indicates that the internal lattice expansion is smaller than the surface lattice expansion. It is also observed from the XRD patterns that the crystal planes at the high-diffraction angle do not change significantly, suggesting that they are less affected by the lattice strain. The HRTEM and XRD results confirm the successful synthesis of Bi_2S_3 with lattice strain.

2.1.2. Structural Characterization and Energy Level Analysis

The TEM image of Bi_2S_3-9.7% is shown in **Figure 2**a, the Bi_2S_3 superstructure is composed of nanorods with a diameter of ≈10 nm, and the angle between adjacent nanorods is ≈90°. From the HRTEM image (Figure 2b), the crystal planes parallel to the rod axis have a lattice spacing of 0.36 nm, corresponding to that of the (130) plane, which indicates that the nanorods have a [001]-directional growth. The corresponding selected area electron diffraction (SAED) pattern (Figure 2c) displays unique four-strong ordered electron diffraction spots, similar to single-crystal diffraction spots, indicating these nanorods have high crystallinity and a preferred growth direction of [001], which is consistent with the HRTEM result. The linearly ordered small spots between strong spots suggest the nanorods are organized to form a structure that has tetragonal symmetry. The four-strong tetragonal electron diffraction spots are calculated to have a d-spacing of 5.56 Å, which are from the periodic crystal planes of (200) of the tetragonally arranged Bi_2S_3 single-crystal nanorods. Furthermore, the tendency of the growth of [001]-oriented Bi_2S_3 nanorods along the two perpendicular [100] and [010] directions is due to the close lattice matching between the *a*- or *b*- axis of tetragonal BiOCOOH (a = b = 3.90 Å) and the *c*-axis of orthorhombic Bi_2S_3 (c = 3.98 Å), which finally leads to the interwoven Bi_2S_3 networks. The high-angle annular dark-field scanning transmission electron microscopy (HAADF-STEM) image and the corresponding element mappings (Figure 2d) confirm the as-prepared Bi_2S_3 only contains Bi and S. The specific surface area of Bi_2S_3-9.7% was measured by nitrogen adsorption/desorption isotherms. As displayed in Figure S3a (Supporting Information), the specific surface area of the sample is 179.13 $m^2\ g^{-1}$, showing a much higher catalytic surface area than that of the commercial Bi_2S_3.[29] The pore volume (Figure S3b, Supporting Information) of Bi_2S_3-9.7% calculated by the Barrett–Joyner–Halenda (BJH) method is 0.102 $cm^3\ g^{-1}$, and the pores are mainly distributed at less than 1, 2.1, and 3.6 nm, confirming the co-existence of micropores

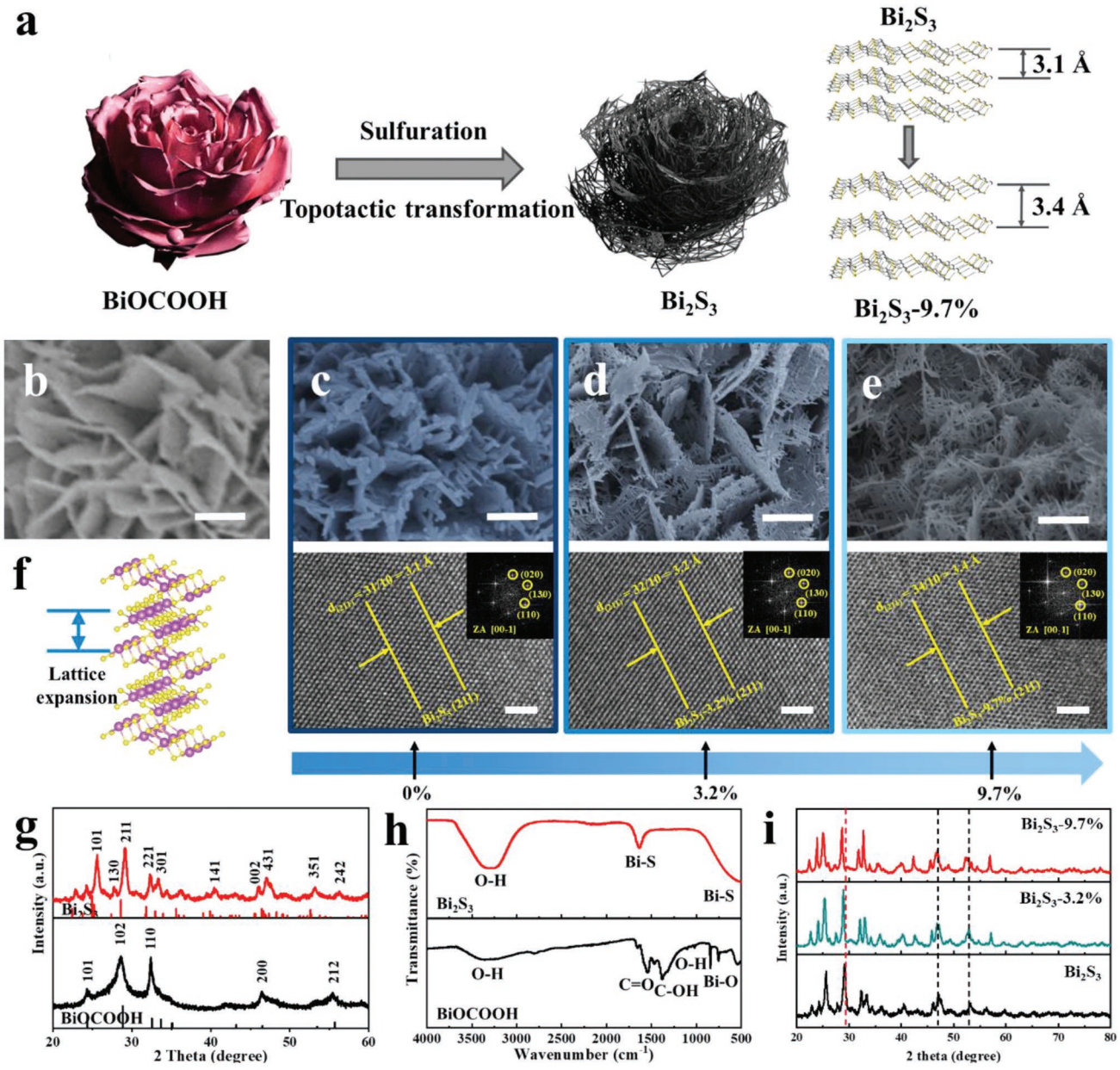

Figure 1. Synthesis and lattice strain analysis of Bi_2S_3. a) Schematic diagram of the synthesis of lattice-strained Bi_2S_3. b) SEM image of the BiOCOOH precursor (scale bar: 500 nm). c-e) SEM (top) (scale bar: 500 nm) and HRTEM (bottom) (scale bar: 2 nm) images of Bi_2S_3 without lattice strain and with lattice strains of 3.2% and 9.7%, respectively (insets: SAED patterns corresponding to the HRTEM images). f) Schematic of the crystal structure variation of Bi_2S_3. g) XRD patterns of BiOCOOH and Bi_2S_3. h) FT-IR spectra of BiOCOOH and Bi_2S_3. i) XRD patterns of Bi_2S_3, Bi_2S_3-3.2% and Bi_2S_3-9.7%.

and mesopores. The results indicate the 3D hierarchical structure greatly enhanced the absorption ability and pore structure of the sample.

The energy level diagrams of Bi_2S_3 and Bi_2S_3-9.7% are derived from the XPS valence band and UV–vis absorption spectra, as shown in Figure 2e,f and Figure S4 (Supporting Information). The valence band maxima of Bi_2S_3 and Bi_2S_3-9.7% are 1.01 and 1.84 eV, and the bandgaps are 1.66 and 0.64 eV, respectively. From the energy level diagram, it is seen that the bandgap is decreased by interlayer swelling, indicating the lattice strain enhances the conductivity of the sample.

2.2. Evaluation of the Hydrogen Evolution Performance

The lattice strain alters the local atomic and electronic environment in the Bi_2S_3 samples, thereby affecting their catalytic activity. The electrocatalytic HER activities were evaluated in 0.5 M H_2SO_4, 1 M KOH, and 1 M PBS electrolyte using a three-electrode system, all potentials quoted are versus reversible hydrogen electrode (RHE). As shown in **Figure 3**a–c and Table S1 (Supporting Information) in acidic solution, the required overpotentials for Bi_2S_3-9.7% are 22, 91, and 127 mV to reach an anodic current density of 10, 50, and 100 mA cm^{-2},

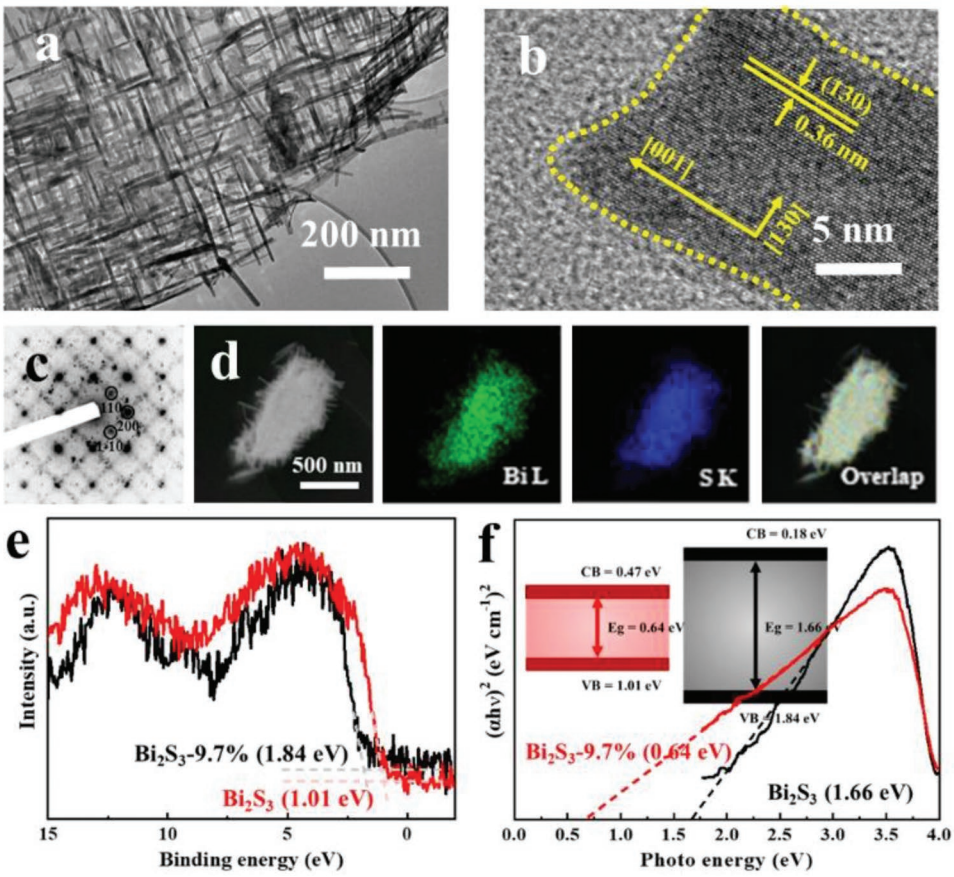

Figure 2. Structural characterization and energy level structure of the lattice-strained Bi_2S_3. a) TEM, b) HRTEM images, and c) the corresponding SAED pattern of Bi_2S_3-9.7%. d) HAADF-STEM image and EDS-mapping images of Bi_2S_3-9.7%. e) Valence band XPS spectra of Bi_2S_3 and Bi_2S_3-9.7%. f) Tauc plots of Bi_2S_3 and Bi_2S_3-9.7% (Inset: energy level diagrams).

respectively, which are much lower than those of Bi_2S_3 (81, 161, and 220 mV) and Bi_2S_3-3.2% (52, 118, and 163 mV). The fitted value of Tafel slope for Bi_2S_3-9.7% is 72.6 mV dec^{-1}, much smaller than those of Bi_2S_3 (91.4 mV dec^{-1}) and Bi_2S_3-3.2% (77.2 mV dec^{-1}). The observed Tafel slope of Bi_2S_3-9.7% suggests that the mechanism of HER is Volmer ($H_3O^+ + e^- + * \rightarrow H^* + H_2O$) – Heyrovsky ($H_3O^+ + e^- + H^* \rightarrow H_2 + H_2O + e^-$).[30,31] Bi_2S_3-9.7% also exhibits the best performance among the samples in both alkaline and neutral electrolytes (Figure 3d–i; Tables S2 and S3, Supporting Information), the overpotentials at 10, 50, and 100 mA cm^{-2} are 74, 143, and 175 mV in 1 M KOH, and 96, 209, 269 mV in 1 M PBS, and the Tafel slopes are 73.8 and 87.2 mV dec^{-1} in alkaline and neutral solutions, respectively. While the overpotentials of Bi_2S_3 and Bi_2S_3-3.2% at 10, 50, and 100 mA cm^{-2} are 128, 186, 228 mV and 177, 327, 397 mV in 1 M KOH, respectively, and 158, 280, 354 mV and 243, 361, 425 mV in 1 M PBS, respectively. The Tafel slopes of Bi_2S_3 and Bi_2S_3-3.2% are 81.4 and 107.5 mV dec^{-1} in alkaline electrolyte, and 90.1 and 95.9 mV dec^{-1} in alkaline electrolyte, respectively (Figure 3d–i; Tables S2 and S3, Supporting Information). The similar values of Tafel slopes for the Bi_2S_3 samples indicate the Volmer–Heyrovsky mechanism across the pH range. The Tafel slopes in acidic media are smaller than those in alkaline and neutral electrolytes because the Volmer step requires a large amount of activation energy in alkaline and neutral solutions, which leads to relatively slower HER reaction kinetics.[32]

In view of the good activity in all pH media, the Bi_2S_3 samples were tested for HER performance in seawater (**Figure 4**a,b; Table S4, Supporting Information). Bi_2S_3-9.7% exhibits far better catalytic activity than the other samples, showing the lowest overpotentials (η_{10} = 126 mV, η_{50} = 221 mV, η_{100} = 303 mV) and the lowest Tafel slope (85.1 mV dec^{-1}), further proving the activity enhancement from lattice strain. The presence of lattice strain also prolongs the electrocatalytic HER stability of Bi_2S_3-9.7% in seawater, and there is no degradation in performance after 60 h (Figure 4c). The N,N-diethyl-p-phenylenediamine (DPD) method is used to detect the possible formation of Cl-oxidation products (ClO^-) during the test (Figure 4c, inset). No color change indicates no production of the hypochlorite that corrodes the catalyst.[33,34] The intrinsic catalytic activity of the Bi_2S_3 samples is evaluated by determining the electrochemically active surface area (ECSA) and mass activity. ECSA is proportional to the double-layer capacitance (C_{dl}), which is obtained and calculated from cyclic voltammetry (CV) curves, as shown in Figure 4d and Figure S5 (Supporting Information). The C_{dl} of Bi_2S_3-9.7% is 50.25 mF cm^{-2}, much higher than those of Bi_2S_3 (42.75 mF cm^{-2}) and Bi_2S_3-3.2% (34.25 mF cm^{-2}). The mass

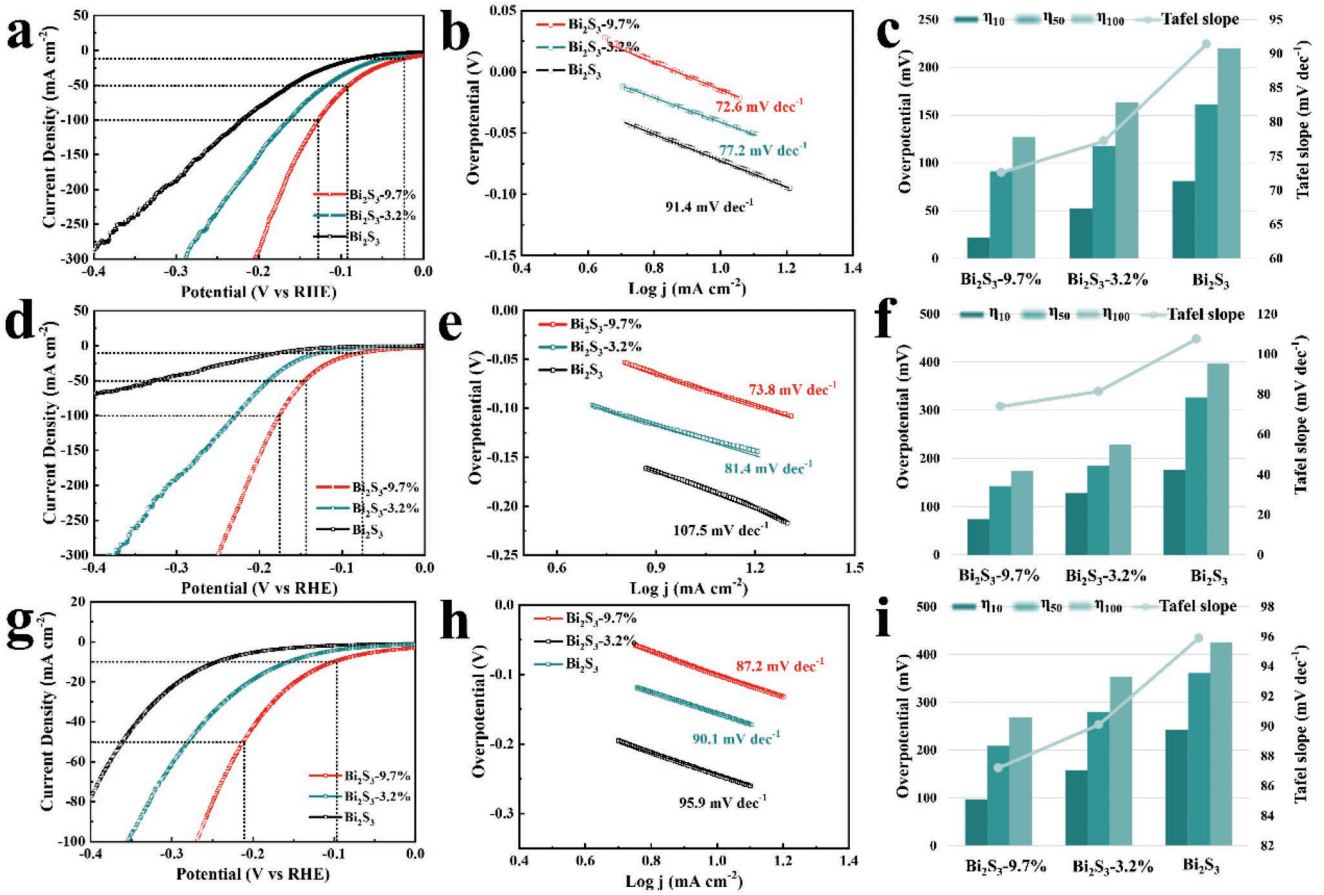

Figure 3. Evaluation of HER performance in all-pH solutions. a) Hydrogen evolution polarization curves, b) Tafel plots, and c) their comparisons of Bi_2S_3 with different lattice strains in acidic solution. d) Hydrogen evolution polarization curves, e) Tafel plots, and f) their comparisons of Bi_2S_3 with different lattice strains in alkaline solution. g) Hydrogen evolution polarization curves, h) Tafel plots, and i) their comparisons of Bi_2S_3 with different lattice strains in neutral solution.

activity of Bi_2S_3-9.7% at an overpotential of 60 mV in freshwater is 80.3 A g^{-1} (Figure 4e), which is ≈ five times and two times higher than that of Bi_2S_3 and Bi_2S_3-3.2%, respective, which implies that the lattice strain increases the catalytic activity. In addition, the electrolyte contact angle test demonstrates that the Bi_2S_3 with the largest lattice swelling (Bi_2S_3-9.7%) has the highest hydrophilicity (Figure 4f), indicating that the lattice expansion effectively increases the contact between reactants and solvent molecules, leading to a better catalytic performance. The remarkable HER activity of the as-obtained Bi_2S_3-9.7% is superior to most of the state-of-the-art Bi- and S-based non-noble metal HER electrocatalysts previously reported in for all pH electrolytes and seawater (Figure 4g–i; Tables S5–S7, Supporting Information).

2.3. Active Sites for Hydrogen Evolution Catalysis

2.3.1. Interpretation of the Lattice Strain on the Influence of HER Activity

Theoretical simulations were performed to gain further insight into the relationship of the improved electrocatalytic activities and lattice strain. The geometric structures of Bi_2S_3 samples with different lattice strains are shown in **Figure 5**a, these structures were built in consideration of generated lattice strain, and the corresponding bulk moduli were calculated, which is inversely proportional to the experimental lattice strain.[35–37] The calculated density of states (DOS) of Bi_2S_3-9.7% near the Fermi level is higher and the bandgap is smaller compared with those of the other samples (Figure 5b), implying enhanced electron mobility, consistent with the XPS and UV–vis results. The optimized structures and Gibbs free energy diagrams of Bi_2S_3 samples for HER in acidic solution are shown in Figure 5c. It is observed that the $|\Delta G_{H^*}|$ of Bi_2S_3-9.7% (–0.28 eV) is much smaller and closer to the optimal value of zero than those of Bi_2S_3 (–0.89 eV) and Bi_2S_3-3.2% (–0.53 eV), revealing the favorable H* adsorption after the introduction of lattice strain. The optimized structures and free energy diagrams in alkaline and neutral solutions are displayed in Figure 5d, in which the dissociation of water is pivotal. The energy barrier for water dissociation in the Volmer reaction on the surface of Bi_2S_3-9.7% is 0.67 eV, which is lower than those of Bi_2S_3 (1.09 eV) and Bi_2S_3-3.2% (0.88 eV), and the barriers on the Heyrovsky step for Bi_2S_3-9.7%, Bi_2S_3-3.2%, and Bi_2S_3 are 1.12, 1.45, and 1.63 eV, respectively. The relatively lower barriers of Bi_2S_3-9.7%

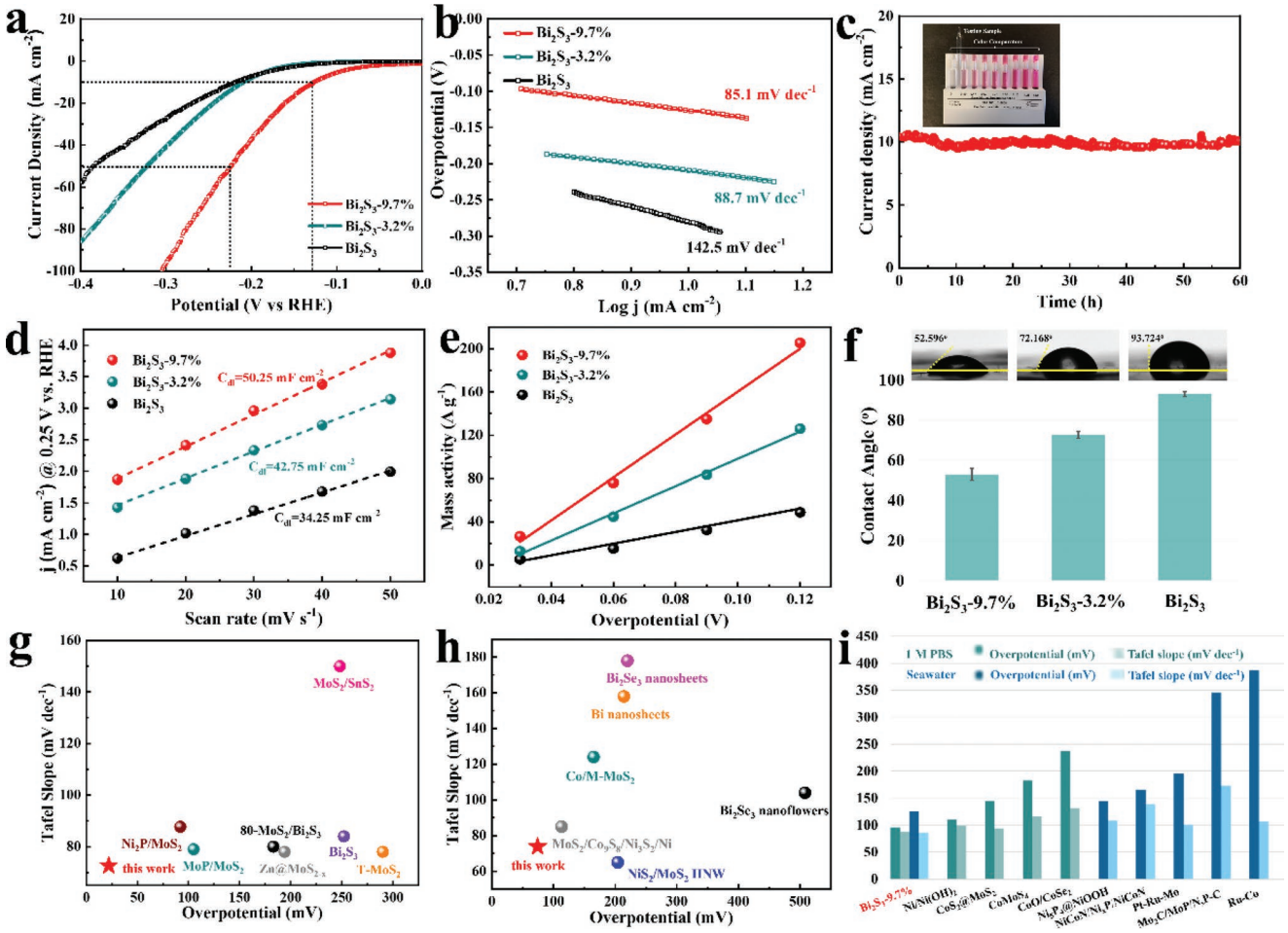

Figure 4. Evaluation of HER performance in seawater. a) Hydrogen evolution polarization curves, b) Tafel plots of Bi_2S_3 with different lattice strains in seawater. c) Chronoamperometry stability test at an applied potential of 0.13 V. (inset: hypochlorite detection result of the electrolyte after seawater HER stability test.) d) Capacitive current of Bi_2S_3 with different lattice strains measured at 0.25 V as a function of scan rate. e) Mass activity of Bi_2S_3 with different lattice strains. f) Electrolyte contact angles of Bi_2S_3 with different lattice strains. Comparisons of HER activities with some recently reported Bi-based and S-based catalysts in g) acidic solution, h) alkaline solution, i) neutral solutions, and seawater, respectively.

indicate the promoted water dissociation kinetics on the sample with high lattice strain. Furthermore, the influence of lattice strain on Bi 3d orbital configuration was investigated. With the increase of the lattice strain, the Bi 3*d* band width decreases, and the *d*-band center shifts positively compared to the Fermi level, implying that the generated strain greatly alters the electronic properties (Figure 5e). A scheme of the changes of the band structures in the samples with lattice strain is shown in Figure 5f. The lattice strain gives rise to a decreased bandwidth and an uplift of the Bi 3*d*-band center, promoting the electron exchange with the S 2*p* orbits, leading to greater covalencies in the Bi—S bond and enhancing the binding of hydrogen intermediates with neighboring Bi atoms, which is conducive to the improvement of hydrogen evolution catalytic activities.

2.3.2. Post-Mortem Investigations after HER

To understand the catalytically active sites that produce the extraordinary HER activity of the Bi_2S_3 catalyst with lattice strain, the microstructure, chemical composition and valence state evolution of Bi_2S_3-9.7% after the HER test (Bi_2S_3-9.7%-A) in alkaline electrolyte were studied. The SEM image, TEM image, and corresponding SAED pattern of Bi_2S_3-9.7% after HER show that the hierarchical structure with interwoven nanorods is maintained, indicating its great structural stability (**Figure 6**a–c). However, it can be seen from the HRTEM images (Figure 6d,e) that a pseudo-amorphous structure is formed on the outside of the nanorods after HER, and the lattice spacing is reduced to 3.3 Å, corresponding to a lattice expansion of 6.4%, indicating a decrease of lattice strain during the test. The XRD test was performed on the sample after HER (Figure 6f), by comparing with the XRD pattern of Bi_2S_3-9.7%, a peak appearing at 30.6° corresponding to Bi, indicating that Bi reduction occurs during the test (JCPDS card No. 51–0765), suggesting that the structure at the edge of the Bi_2S_3 nanorods observed in post-mortem studies is quasi-crystalline Bi metal. Shift to high angle in the XRD pattern of Bi_2S_3-9.7%-A is also observed, indicating that the lattice expansion is reduced, consistent with the HRTEM result. The blue-shift of the Bi—S band

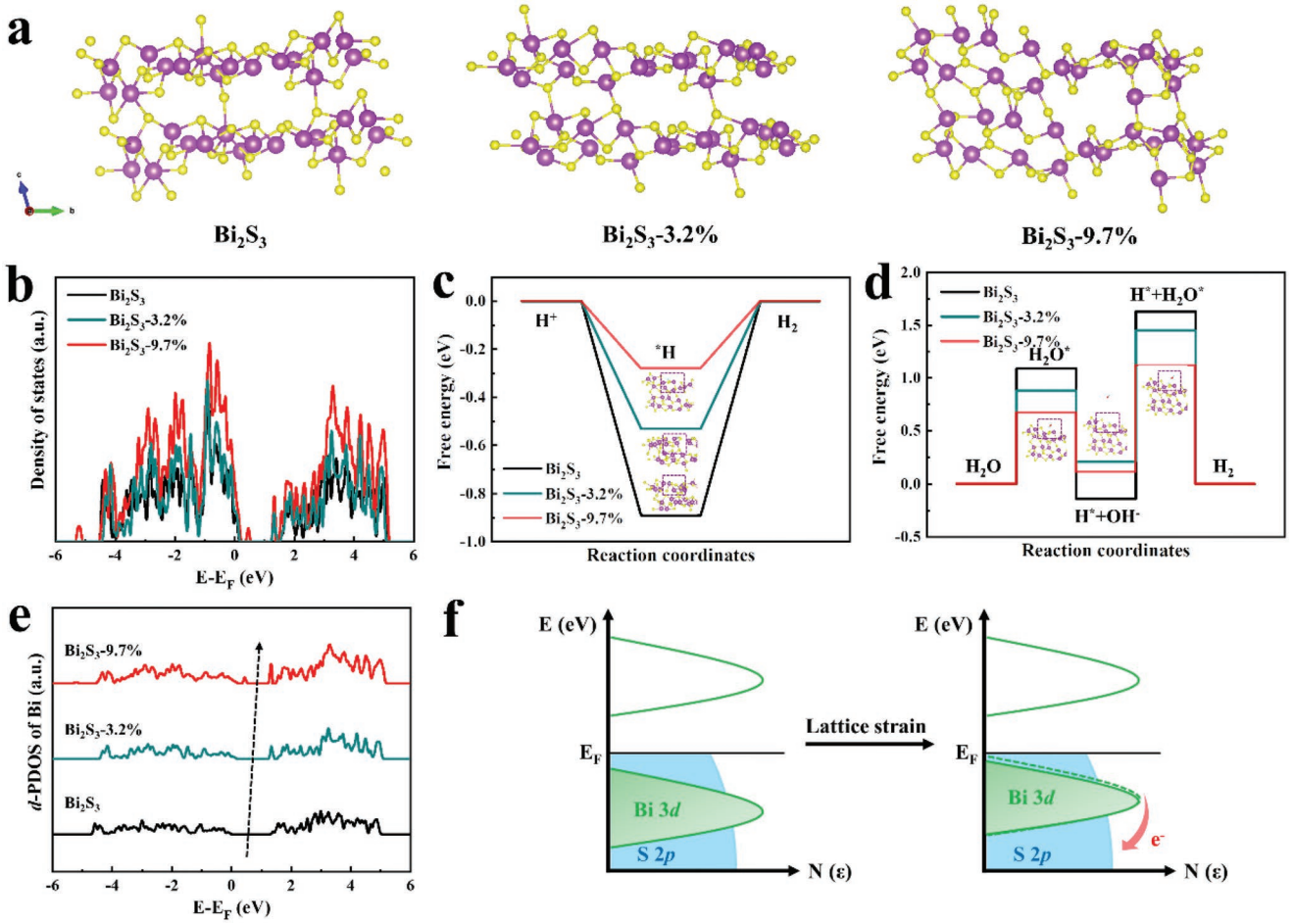

Figure 5. Interpretation of the lattice strain on the influence of HER activity. a) The geometric structures and b) electronic structure of Bi_2S_3 samples with different lattice strains. c) The optimized structures and Gibbs free energy diagrams of HER in an acidic medium. d) The optimized structures and Gibbs free energy diagrams of HER in alkaline and neutral media. e) The d-orbital partial density of states (*d*-PDOS) of Bi in the Bi_2S_3 samples. f) Schematic of the electron exchange for Bi_2S_3-9.7%.

in FT-IR reveals that the reduced lattice expansion shortens the bond length of Bi—S (Figure 6g).[38–40] The fitted Bi 4f spectra of Bi_2S_3 with different lattice strains before and after HER were compared using XPS (Figure 6h; Figure S6, Supporting Information) and found that the chemical composition of the Bi_2S_3 sample without lattice strain remained basically unchanged before and after the HER test. With the increase of lattice strain, a new metallic Bi^0 peak appeared in the fitted Bi 4*f*, which is consistent with the results of HRTEM and XRD, confirming the generation of Bi in the samples with lattice strain after HER.[41,42]

Operando Raman spectroscopy was further performed on the Bi_2S_3 catalysts to explore the effect of lattice strain on the change of valence state in the real-time HER process (**Figure 7**). As the voltage alters from 0 to −0.2 V versus RHE, the strain-free catalyst remains stable, and the peaks at 123 and 139 cm^{-1} are attributed to the E_g and A_{1g} stretching modes of Bi—S bonds, respectively (Figure 7a).[43–45] For the strain-containing Bi_2S_3, the characteristic vibration of Bi—S band gradually weakened, and a new band appeared at 96 cm^{-1}, corresponding to the A_{1g} stretching modes of Bi—Bi bonds (Figure 7b,c).[46,47] In addition, the self-reconstruction of the samples with high strain is more obvious, the time of this process for Bi_2S_3-9.7% is shorter compared with that of Bi_2S_3-3.2%, and the new Bi—Bi bands are also stronger for Bi_2S_3-9.7%, which shows that the lattice strain is beneficial in the self-reconstruction and production of Bi during HER.

By combining ex situ electron microscopy with Operando Raman spectroscopy, it is concluded that lattice strain plays a key role in triggering surface reconstruction and the reduction of Bi_2S_3 under applied negative potential, and the in situ generated Bi-metallic phase are the active sites for the HER process.

2.4. Capacitive Performance of Bi_2S_3-9.7% after HER

2.4.1. Charge Storage Kinetics of Bi_2S_3-9.7% after HER

Bi_2S_3 has been widely used as an electrode in supercapacitors due to its low price and high theoretical capacity, however, its supercapacitive performance is limited by the low electrical conductivity and self-aggregation during the test.[48–53] The

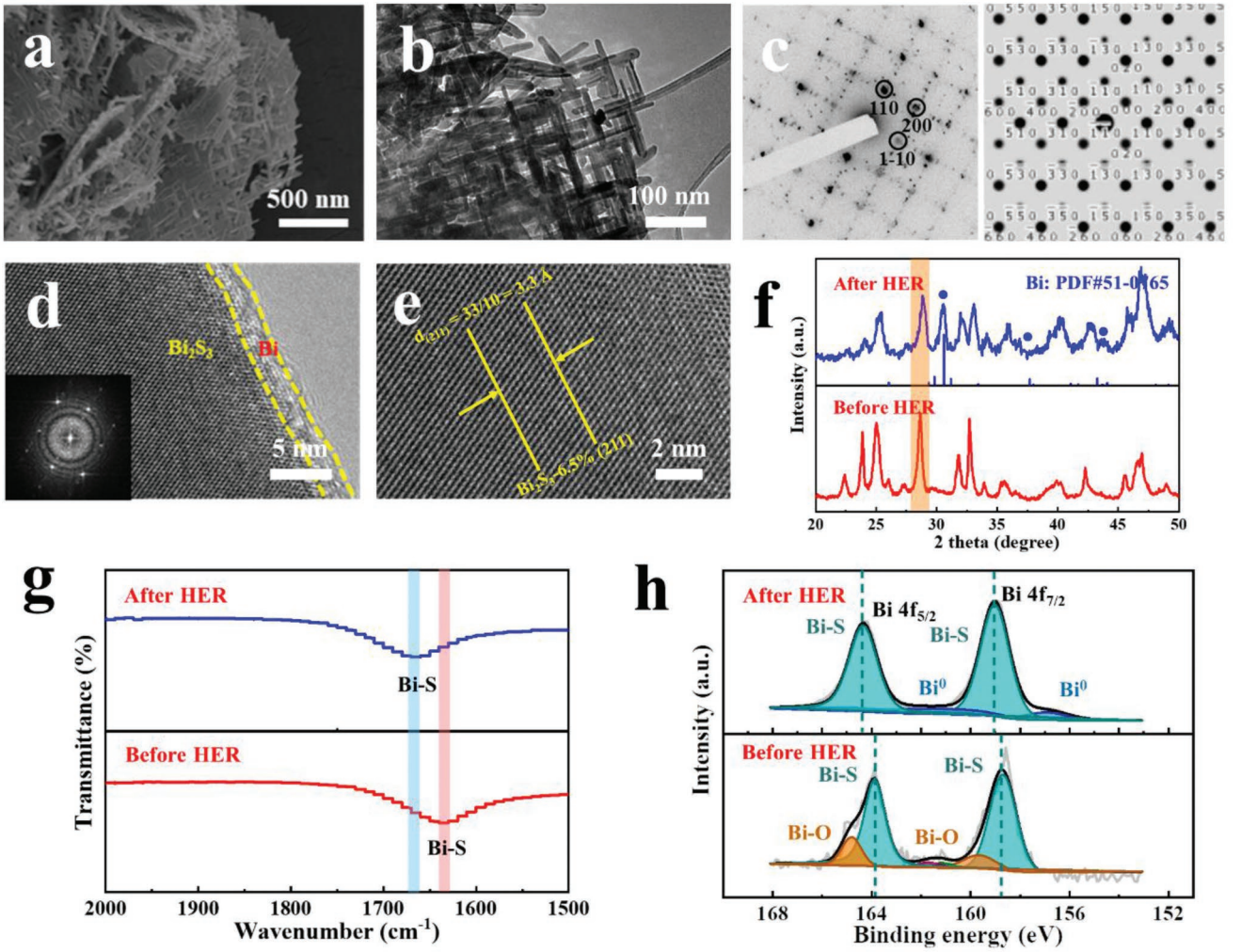

Figure 6. Active sites for hydrogen evolution catalysis. a) SEM, b) TEM, c) corresponding SAED pattern (left) and simulated SAED pattern (right) of Bi_2S_3-9.7% after HER in alkaline solution. d,e) HRTEM of Bi_2S_3-9.7% after HER in alkaline solution (Inset: corresponding SAED pattern). f) XRD patterns of Bi_2S_3-9.7% before and after HER in alkaline solution. g) FT-IR spectra of Bi_2S_3-9.7% before and after HER in alkaline solution. h) XPS of Bi_2S_3-9.7% before and after HER in alkaline solution. All the spectra were shown with raw data and fitting data derived by Lorentz–Gaussian function.

Bi_2S_3-9.7% catalyst after HER (Bi_2S_3-9.7%-A) demonstrates good structural stability, and its conductivity has been greatly improved due to the introduction of lattice strain and the in situ generation of metallic Bi by reduction during the HER process. In view of the benefits discussed above, the supercapacitive behaviors of the Bi_2S_3-9.7%-A electrode have been investigated in a three-electrode configuration in 3 M KOH electrolyte.

Figure 8a shows the CV curves of Bi_2S_3-9.7% electrodes in 3 M KOH before and after HER testing. The Bi_2S_3-9.7%-A electrode exhibits a higher redox current and a larger enclosed area, indicating its enhanced faradic capacitance that results from increased electroactive sites. The redox peaks reveal the reversible conversion between Bi_2S_3 and Bi_2S_3OH in the electrolyte ($Bi_2S_3 + OH^- \rightarrow Bi_2S_3OH + e^-$).[54–58] For Bi_2S_3-9.7%-A, the additional peak area is attributed to the reversible reaction of Bi and Bi_2O_3 ($2Bi + 6OH^- \rightarrow Bi_2O_3 + 3H_2O + 6e^-$), the electron transfer number of Bi is significantly higher than that of Bi_2S_3, greatly increasing the capacitance. Figure 8b displays the CV curves of Bi_2S_3-9.7%-A electrode at scan rates of 5–25 mV s^{-1}. As the scan rate increases, the peak current response increases, and the oxidation and reduction peaks shift positive and negative, respectively, which is due to the electrochemical polarization and internal resistance of the electrode.

To further study the enhanced supercapacitive behavior of Bi_2S_3-9.7%-A, the CV curve is analyzed. The power law was applied to scrutinize the diffusion-controlled and surface capacitive contributions of current, which is expressed as $i_p = a \times v^b$, where i_p is the peak current (A cm^{-2}), v is the scan rate (V s^{-1}), a and b are the adjustable parameters.[47] A b-value of 0.5 indicates a diffusion-controlled process, whereas a b-value of 1 suggests surface capacitive behavior.[55] The b-values of cathodic and anodic peaks calculated from the slopes of the linear fit of $\log(i)$ versus $\log(v)$ are 0.60 and 0.53, respectively (Figure 8c), suggesting the current response of Bi_2S_3-9.7%-A electrode is dominated by diffusion-controlled behavior. Figures S7 and S8 (Supporting Information)show the linear fit of $v^{1/2}$ versus $i/v^{1/2}$ for Bi_2S_3-9.7%-A electrode. To quantify the relative contribution of the diffusion-controlled

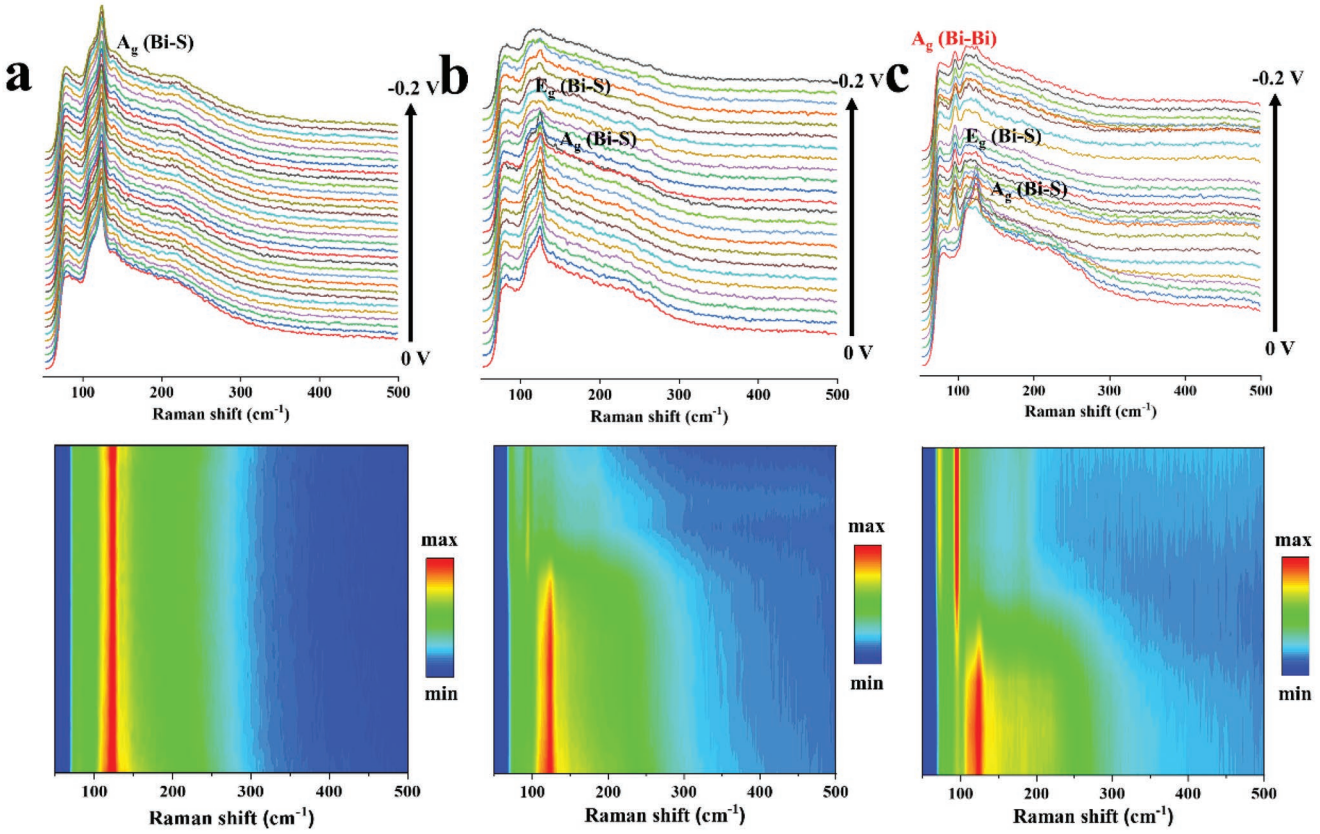

Figure 7. Active sites for hydrogen evolution catalysis. Operando Raman spectra and the corresponding contour plot of a) Bi_2S_3, b) Bi_2S_3-3.2%, and c) Bi_2S_3-9.7% obtained from the voltage changing from 0 to –0.2 V (vs RHE).

and surface capacitive mechanisms, the power law is modified as $i_p = k_1\nu + k_2\nu^{1/2}$, where it is changed as $i_p/\nu^{1/2} = k_1\nu^{1/2} + k_2$, where i_p is the peak current (A cm^{-2}), ν is the scan rate (V s^{-1}), k_1 and k_2 are current contributions from surface capacitive and diffusion-controlled behavior, respectively.[59–63] The relative current contributions obtained according to the above equations are displayed in Figure 8d. It is observed that at a low scan rate of 5 mV s^{-1}, the diffusion-controlled contribution (87.4%) is much higher than the capacitive current contribution (12.6%). With an increase in the scan rate, the surface capacitive contribution of the fast kinetics process gradually increases, reaching 28.3% at a high scan rate of 25 mV s^{-1}, while it is still lower than the current contribution of the diffusion-controlled process (71.7%). This indicates that the charge storage capacity of the Bi_2S_3-9.7%-A electrode is mainly derived from faradaic behavior.

2.4.2. Capacitive Performance of Bi_2S_3-9.7%-A//AC Asymmetric Supercapacitor

Encouraged by the excellent electrochemical capacitive performance of Bi_2S_3-9.7%-A, an asymmetric supercapacitor (ASC) was assembled using Bi_2S_3-9.7%-A as the positive electrode and activated carbon (AC) as the negative electrode, as shown in Figure 8e. Figure 8f displays the CV curves of the Bi_2S_3-9.7%-A//AC ASC measured at scan rates between 10 and 50 mV s^{-1} across a potential window of 0–1.5 V. It is observed that the CV curves of Bi_2S_3-9.7%-A //AC ASC exhibit ideal capacitive and faradaic behaviors as the scan rate increases, which shows its good electrochemical reversibility and the benefits of the combination of double-layer capacitive and faradaic mechanisms.

Figure 8g displays the galvanostatic charge–discharge (GCD) curves performed at different current densities of 1–32 A g^{-1}. Bi_2S_3-9.7%-A//AC ASC exhibits high gravimetric capacitance of 307 and 133 F g^{-1} at current densities of 1 and 30 A g^{-1}, superb capacitance and rate capability, much better than that of Bi_2S_3-9.7%//AC ASC (Figure 8h; Figure S9, Supporting Information). This demonstrates that the in situ generated Bi-metal on the fringe of the Bi_2S_3 nanorods greatly enhances the charge storage ability. The comparison of energy and power density with data previously reported is presented in the Ragone plot (Figure 8i). Bi_2S_3-9.7%-A//AC ASC reaches an excellent energy density of 109 Wh kg^{-1} at a power density of 984 W kg^{-1}, and even maintains 47 Wh kg^{-1} at a high-power density of 24.4 kW kg^{-1}. The energy storage capacities of Bi_2S_3-9.7%-A// AC ASC are much higher than those of the reported Bi_2S_3-based ASC devices (Figure 8i,j; Table S8, Supporting Information). The EIS curves and equivalent circuit of Bi_2S_3-9.7%-A//AC ASC are shown in Figure 8k, suggesting a low charge transfer resistance (R_{ct}), which indicates that the device has good charge transfer kinetics.[52] The long-term cycling performance evaluated at 1 A g^{-1} shows the device has good durability with a capacitance retention of 84.1% after 10 000 cycles.

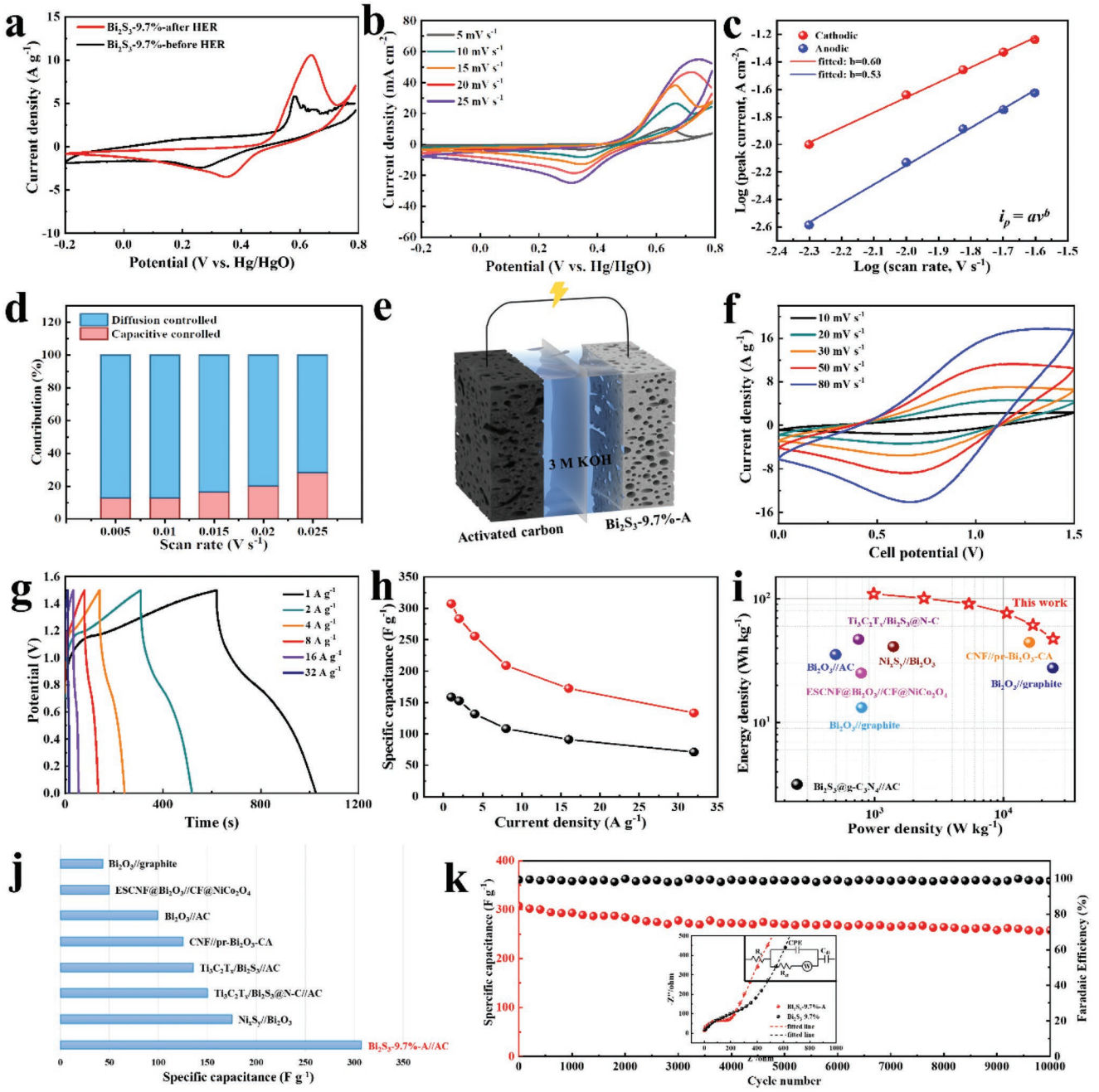

Figure 8. Capacitive Performance of Bi_2S_3-9.7% after HER. a) CV curves of Bi_2S_3-9.7% before and after HER in alkaline solution. b) CV curves of Bi_2S_3-9.7% after HER measured at different scan rates of 5–25 mV s^{-1}. c) The power–law dependence of cathodic and anodic peak currents of Bi_2S_3-9.7% after HER from CV curves. d) Histograms of the capacitive and diffusion-controlled battery-type current contribution of Bi_2S_3-9.7% after HER at different scan rates. e) Schematic illustration of the assembled Bi_2S_3-9.7%-A//AC ASC. f) CV, and g) GCD curves of Bi_2S_3-9.7%-A//AC ASC at various scan rates and current densities. h) Calculated specific capacitance for Bi_2S_3-9.7%//AC ASC and Bi_2S_3-9.7%-A//AC ASC at various current densities. i) Ragone plot of Bi_2S_3-9.7%-A//AC ASC. j) Comparisons of the capacitive performance with some recently reported Bi-based catalysts in alkaline electrolyte. k) Cycling stability of the assembled Bi_2S_3-9.7%-A//AC ASC at the constant current density of 1 A g^{-1} (Inset: Nyquist plots and the corresponding equivalent circuit of Bi_2S_3-9.7%-A//AC ASC).

3. Conclusions

In summary, a novel method for the preparation of 3D hierarchical Bi_2S_3 architectures with tunable lattice strain is reported. The lattice spacing is confirmed to be expanded with the prolongation of sulfuration. The results of XPS valence band spectra and UV–vis show that the bandgap decreases as the lattice strain increases. The as-prepared Bi_2S_3 electrocatalyst with 9.7%-lattice strain exhibits the best HER performance among the Bi_2S_3 samples, exhibiting 22 and 91, 74 and 143, 96 and 209, 126 and 221 mV in acidic, alkaline, neutral electrolytes and simulated seawater, with excellent stability for 60 h test in seawater.

DFT simulations reveal that the lattice strain reduces the bandwidth and upshifts the band center of Bi 3*d* orbits, which promotes the electron exchange with the S 2*p* orbits, favoring the adsorption of H* kinetics and reducing the energy barrier of water dissociation for HER activities. Post-mortem characterizations reveal the formation of pseudo-amorphous Bi on the boundary of Bi_2S_3-9.7% nanorods after HER, which significantly enhances its capacitance. Bi_2S_3-9.7%-A is constructed as an electrode in the ASC, and the as-prepared Bi_2S_3-9.7%-A//AC ASC displays both high energy and power densities in a wide specific capacitance range and shows good retention of 84.1% after 10 000 cycles at 1 A g^{-1}. This work provides valuable guidance for lattice strain regulation of 2D layered sulfide materials for clean energy conversion and storage applications.

Supporting Information

Supporting Information is available from the Wiley Online Library or from the author.

Acknowledgements

H.Z. acknowledges the Imperial College London and China Scholarship Council for the IC-CSC joint scholarship, EPSRC Centre for Doctoral Training in the Advanced Characterization of Materials (EP/L015277/1). The authors acknowledge the use of characterization facilities within the Harvey Flower Electron Microscopy Suite at the Department of Materials, Imperial College London. The authors acknowledge the computational resources provided by the Texas Advanced Computing Center and the National Energy Research Scientific Computing Center.

Conflict of Interest

The authors declare no conflict of interest.

Data Availability Statement

The data that support the findings of this study are available in the supplementary material of this article.

Keywords

asymmetric supercapacitors, bismuth sulfide, lattice strain, pH universal, seawater hydrogen evolution reaction

Received: May 25, 2022
Revised: August 19, 2022
Published online: September 23, 2022

[1] M. Armand, J.-M. Tarascon, *Nature* **2008**, *451*, 652.
[2] A. Vojvodic, J. K. Norskov, *Science* **2011**, *334*, 1355.
[3] Z. Liu, J. Liang, S. Li, S. Peng, Y. Qian, *Chem. - Eur. J.* **2004**, *10*, 634.
[4] Z. Liu, Y. Pei, H. Geng, J. Zhou, X. Meng, W. Cai, W. Liu, J. Sui, *Nano Energy* **2015**, *13*, 554.
[5] R. Wu, Q. Tao, W. Dang, Y. Liu, B. Li, J. Li, B. Zhao, Z. Zhang, H. Ma, G. Sun, X. Duan, X. Duan, *Adv. Funct. Mater.* **2019**, *29*, 1806611.
[6] R. Xu, R. Wu, Y. M. Shi, J. F. Zhang, B. Zhang, *Nano Energy* **2016**, *24*, 103.
[7] I. S. Kwon, I. H. Kwak, T. T. Debela, H. G. Abbas, Y. C. Park, J. Ahn, J. Park, H. S. Kang, *ACS Nano* **2020**, *14*, 6295.
[8] C. Hu, E. Song, M. Wang, W. Chen, F. Huang, Z. Feng, J. Liu, J. Wang, *Adv. Sci.* **2020**, *8*, 2001881.
[9] Y. Hu, L. Mao, X. Yuan, J. Lu, R. Chen, T. Chen, W. Zhang, X. Xue, W. Yan, M. Shokouhimehr, X. Zhang, Z. Jin, *Nano Res.* **2020**, *13*, 2226.
[10] W. Zhang, S. Yang, M. Jiang, Y. Hu, C. Hu, X. Zhang, Z. Jin, *Nano Lett.* **2021**, *21*, 2650.
[11] W. Zhang, Y. Hu, L. Ma, G. Zhu, P. Zhao, X. Xue, R. Chen, S. Yang, J. Ma, J. Liu, Z. Jin, *Nano Energy* **2018**, *53*, 808.
[12] W. P. Utomo, M. K. H. Leung, Z. Yin, H. Wu, Y. H. Ng, *Adv. Funct. Mater.* **2022**, *32*, 2106713.
[13] Y. Wan, H. Zhou, M. Zheng, Z.-H. Huang, F. Kang, J. Li, R. Lv, *Adv. Funct. Mater.* **2021**, *31*, 2100300.
[14] X. Xue, R. Chen, C. Yan, Y. Hu, W. Zhang, S. Yang, L. Ma, G. Zhu, Z. Jin, *Nanoscale* **2019**, *11*, 10439.
[15] J. Qiu, M. Li, J. Xu, X. Zhang, J. Yao, *J. Hazard. Mater.* **2020**, *389*, 121858.
[16] W. Yang, J. Yang, K. Zhao, Q. Gao, L. Liu, Z. Zhou, S. Hou, X. Wang, G. Shen, X. Pang, Q. Xu, Z. Wei, *Adv. Sci.* **2021**, *8*, 2100075.
[17] J. H. Wang, W. Cui, Q. Liu, Z. C. Xing, A. M. Asiri, X. P. Sun, *Adv. Mater.* **2016**, *28*, 215.
[18] I. S. Amiinu, Z. Pu, X. Liu, K. A. Owusu, H. G. R. Monestel, F. O. Boakye, H. Zhang, S. Mu, *Adv. Funct. Mater.* **2017**, *27*, 1702300.
[19] M. Hafeez, L. Gan, H. Li, Y. Ma, T. Zhai, *Adv. Funct. Mater.* **2016**, *26*, 4551.
[20] X. He, F. Liu, P. Hu, W. Fu, X. Wang, Q. Zeng, W. Zhao, Z. Liu, *Small* **2015**, *11*, 5423.
[21] M. Jin, H. Zhang, J. Wang, X. Zhong, N. Lu, Z. Li, Z. Xie, M. J. Kim, Y. Xia, *ACS Nano* **2012**, *6*, 2566.
[22] S. Yang, F. Liu, C. Wu, S. Yang, *Small* **2016**, *12*, 4028.
[23] K. D. Gilroy, X. Yang, S. Xie, M. Zhao, D. Qin, Y. Xia, *Adv. Mater.* **2018**, *30*, 1706312.
[24] Q. Jia, W. Liang, M. K. Bates, P. Mani, W. Lee, S. Mukerjee, *ACS Nano* **2015**, *9*, 387.
[25] J. Yang, J. Yang, J. Y. Ying, *ACS Nano* **2012**, *6*, 9373.
[26] C. Zhu, J. Zeng, J. Tao, M. C. Johnson, I. Schmidt-Krey, L. Blubaugh, Y. Zhu, Z. Gu, Y. Xia, *J. Am. Chem. Soc.* **2012**, *134*, 15822.
[27] Y. He, X. P. Han, D. W. Rao, Y. D. Zhang, J. Zhao, C. Zhong, W. B. Hu, W. F. Wei, Y. D. Deng, *Nano Energy* **2019**, *61*, 267.
[28] M. Shao, F. Ning, M. Wei, D. G. Evans, X. Duan, *Adv. Funct. Mater.* **2014**, *24*, 580.
[29] F. Chang, S. Peng, W. Yan, C. Yang, S. Li, X. Liu, *Colloids Surf. A: Physicochem. Eng. Asp.* **2021**, *610*, 125640.
[30] J. Chen, J. Liu, J. Xie, H. Ye, X. Fu, R. Sun, C. Wong, *Nano Energy* **2019**, *56*, 225.
[31] H. Zhang, S. Geng, M. Ouyang, M. Mao, F. Xie, D. J. Riley, *Small* **2021**, *17*, 2106391.
[32] Y. Li, H. Zhang, M. Jiang, Q. Zhang, P. He, X. Sun, *Adv. Funct. Mater.* **2017**, *27*, 1702513.
[33] Z. P. Wu, X. F. Lu, S. Q. Zang, X. W. Lou, *Adv. Funct. Mater.* **2020**, *30*, 1910274.
[34] H. Zhang, Q. Jiang, J. H. L. Hadden, F. Xie, D. J. Riley, *Adv. Funct. Mater.* **2021**, *31*, 2008989.
[35] J.-S. Kim, H.-K. Kim, S.-H. Kim, I. Kim, T. Yu, G.-H. Han, K.-Y. Lee, J.-C. Lee, J.-P. Ahn, *ACS Nano* **2019**, *13*, 4761.
[36] L. Gan, S. Rudi, C. Cui, M. Heggen, P. Strasser, *Small* **2016**, *12*, 3189.
[37] B. Kang, Y. Kim, W. J. Yoo, C. Lee, *Small* **2018**, *14*, 1802593.
[38] K. Sun, T. Cheng, L. Wu, Y. Hu, J. Zhou, A. Maclennan, Z. Jiang, Y. Gao, W. A. Goddard, Z. Wang, *J. Am. Chem. Soc.* **2017**, *139*, 15608.
[39] Q. Zeng, J. Bai, J. Lia, Y. Lia, X. Lia, B. Zhou, *Nano Energy* **2014**, *9*, 152.
[40] M. Bernal, A. Bagger, F. Scholten, I. Sinev, A. Bergmann, M. Ahmadi, J. Rossmeisl, B. R. Cuenya, *Nano Energy* **2018**, *53*, 27.

[41] L. Li, Y. Liu, J. Y. Dai, H. X. Zhu, A. J. Hong, X. H. Zhou, Z. F. Ren, J. M. Liu, *Nano Energy* **2015**, *12*, 447.
[42] M. S. Shore, J. Wang, A. C. Johnston-Peck, A. L. Oldenburg, J. B. Tracy, *Small* **2011**, *7*, 230.
[43] X. Lu, J. Deng, W. Si, X. Sun, X. Liu, B. Liu, L. Liu, S. Oswald, S. Baunack, H. J. Grafe, C. Yan, O. G. Schmidt, *Adv. Sci.* **2015**, *2*, 1500113.
[44] C. Li, S. Yan, J. Fang, *Small* **2021**, *17*, 2102244.
[45] W. Cheng, X. Zhao, H. Su, F. Tang, W. Che, H. Zhang, Q. Liu, *Nat. Energy* **2019**, *4*, 115.
[46] D. Yao, C. Tang, A. Vasileff, X. Zhi, Y. Jiao, S.-Z. Qiao, *Angew. Chem., Int. Ed.* **2021**, *60*, 18178.
[47] W. Liu, C. F. Guo, M. Yao, Y. Lan, H. Zhang, Q. Zhang, S. Chen, C. P. Opeil, Z. Ren, *Nano Energy* **2014**, *4*, 113.
[48] Y. L. Si, S. Cao, Z. Wu, Y. Ji, Y. Mi, X. Wu, X. Liu, L. Piao, *Nano Energy* **2017**, *38*, 118.
[49] Z. Liu, L. Wang, X. Yu, J. Zhang, R. Yang, X. Zhang, Y. Ji, M. Wu, L. Deng, L. Li, Z. Wang, *Adv. Funct. Mater.* **2019**, *29*, 1807279.
[50] H. Zhang, P. Li, S. Chen, F. Xie, D. J. Riley, *Adv. Funct. Mater.* **2021**, *31*, 2106835.
[51] J. Li, X. Gao, Z. Li, J. Wang, L. Zhu, C. Yin, Y. Wang, X. Li, Z. Liu, J. Zhang, C. Tung, L. Wu, *Adv. Funct. Mater.* **2020**, *31*, 2006030.
[52] J. Qi, Y. Yan, Y. Cai, J. Cao, J. Feng, *Adv. Funct. Mater.* **2021**, *31*, 2008185.
[53] W. Zong, F. Lai, G. He, J. Feng, W. Wang, R. Lian, Y.-E. Miao, G.-C. Wang, I. P. Parkin, T. Liu, *Small* **2018**, *14*, 1801562.
[54] F. Yang, J. Y. Ye, Q. Yuan, X. T. Yang, Z. X. Xie, F. L. Zhao, Z. Y. Zhou, L. Gu, X. Wang, *Adv. Funct. Mater.* **2020**, *30*, 1908235.
[55] L. Wang, N. Nguyen, Z. Shen, P. Schmuki, Y. Bi, *Nano Energy* **2018**, *50*, 331.
[56] S. Liu, L. Zheng, P. Yu, S. Han, X. Fang, *Adv. Funct. Mater.* **2016**, *26*, 3331.
[57] L. Zheng, S. Han, H. Liu, P. Yu, X. Fang, *Small* **2016**, *12*, 1527.
[58] J. He, W. Lv, Y. Chen, K. Wen, C. Xu, W. Zhang, Y. Li, W. Qin, W. He, *ACS Nano* **2017**, *11*, 8144.
[59] P. Yu, Z. Zhang, L. Zheng, F. Teng, L. Hu, X. Fang, *Adv. Energy Mater* **2016**, *6*, 1601111.
[60] X. Liu, L. Zhang, Y. Zheng, Z. Guo, Y. Zhu, H. Chen, F. Li, P. Liu, B. Yu, X. Wang, *Adv. Sci.* **2019**, *6*, 1801898.
[61] Z. Pan, F. Cao, X. Hu, X. Ji, *J. Mater. Chem. A* **2019**, *7*, 8984.
[62] H. Yi, R. Qin, S. Ding, Y. Wang, S. Li, Q. Zhao, F. Pan, *Adv. Funct. Mater.* **2020**, *31*, 6.
[63] K. Krishnamoorthy, P. Pazhamalai, V. K. Mariappan, S. Manoharan, D. Kesavan, S.-J. Kim, *Adv. Funct. Mater.* **2020**, *31*, 2008422.